Upside-down fluxes Down Under: CO$_2$ net sink in winter and net source in summer in a temperate evergreen broadleaf forest

Alexandre A. Renchon[1], Anne Griebel[1], Daniel Metzen[1], Christopher A. Williams[2], Belinda Medlyn[1], Remko A. Duursma[1], Craig VM Barton[1], Chelsea Maier[1], Matthias M. Boer[1], Peter Isaac[3], David Tissue[1], Victor Resco de Dios[4], Elise Pendall[1]

[1]*Hawkesbury Institute for the Environment, Western Sydney University, Penrith, NSW, Australia.*
[2]*Clark University, Graduate School of Geography, Worcester, Massachusetts 01610, USA.*
[3]*CSIRO Oceans & Atmosphere Flagship, Yarralumla, ACT, 2600, Australia.*
[4]*Department of Crop and Forest Sciences and Agrotecnio Center, University of Lleida, E-25198 Lleida, Spain.*

Abstract

Predicting the seasonal dynamics of ecosystem carbon fluxes is challenging in broadleaved evergreen forests because of their moderate climates and subtle changes in canopy phenology. We assessed the climatic and biotic drivers of the seasonality of net ecosystem-atmosphere CO$_2$ exchange (NEE) of a eucalyptus-dominated forest near Sydney, Australia, using the eddy covariance method. The climate is characterized by a mean annual precipitation of 800 mm and a mean annual temperature of 18 °C, hot summers and mild winters, with highly variable precipitation. In the four-year study, the ecosystem was a sink each year (-225 g C m^{-2} y^{-1} on average, with a standard deviation of 108 g C m^{-2} y^{-1}); inter-annual variations were not related to meteorological conditions. Daily net C uptake was always detected during the cooler, drier winter months (June through August), while net C loss occurred during the warmer, wetter summer months (December through February). Gross primary productivity (GPP) seasonality was low, despite longer days with higher light intensity in summer, because vapour pressure deficit (D) and air temperature (T$_a$) restricted surface conductance during summer while winter temperatures were still high enough to support photosynthesis. Maximum GPP during ideal environmental conditions was significantly correlated with remotely sensed enhanced vegetation index (EVI, r^2 = 0.46) and with canopy leaf area index (LAI, r^2 = 0.29), which increased rapidly after mid-summer rainfall events. Ecosystem respiration (ER) was highest during summer in wet soils and lowest during winter months. ER had larger seasonal amplitude compared to GPP, and therefore drove the seasonal variation of NEE. Because summer carbon uptake may become increasingly limited by atmospheric demand and high temperature, and ecosystem respiration could be enhanced by rising temperature, our results suggest the potential for large-scale seasonal shifts in NEE in sclerophyll vegetation under climate change.

Keywords: net ecosystem exchange, seasonal variability, atmospheric demand, canopy phenology

1. Introduction

Forests and semi-arid biomes are responsible for the majority of global carbon storage by terrestrial ecosystems (Dixon et al. 1994; Pan et al. 2011; Poulter et al. 2014; Schimel et al. 2001). Photosynthesis and respiration by these biomes strongly influence the seasonal cycle of atmospheric CO_2 (Baldocchi et al. 2016; Keeling et al. 2001). Continuous measurements of land-atmosphere exchanges of carbon, energy and water provide insights into the seasonality of forest ecosystem processes, which are driven by the interactions of climate, plant physiology and forest composition and structure (Xia et al. 2015). Net ecosystem exchange (NEE) seasonality is relatively well understood in cool-temperate ecosystems; deciduous trees can only photosynthesize when they have leaves and NEE dynamics are thus principally influenced by the phenology of canopy processes. NEE of deciduous forests thus has a more pronounced seasonality than that of evergreen conifer forests at similar latitudes (Novick et al. 2015). For high-latitude evergreen conifer forests, NEE seasonality is strongly limited by cold temperature limitation of photosynthesis (Kolari et al. 2007) and respiration. In contrast, seasonality of NEE in evergreen broadleaf forests, typically occurring in warm-temperate and tropical regions, is much less well understood (Restrepo-Coupe et al. 2017; Wu et al. 2016).

The seasonality of gross primary productivity (GPP) in evergreen broadleaf forests may be driven by climate (e.g. dry/wet seasons) and/or by canopy dynamics (Wu et al. 2016). In tropical evergreen forests, air temperature and day length are similar seasonally, but precipitation seasonality can be strong, with higher radiation and temperature (1 or 2 °C higher) in the dry season (Trenberth 1983; Windsor 1990). Counter-intuitively, GPP can be higher during the dry season, as cloud cover may limit productivity in the wet season (Graham et al. 2003; Hutyra et al. 2007; Saleska et al. 2003). Canopy dynamics can be an important determinant of GPP seasonality in evergreen broadleaf forests; although leaves are present in the canopy year-round in evergreen canopies, LAI may show considerable temporal variability seasonally as new leaves are produced and old leaves die, especially during leaf flush and senescence periods (Duursma et al. 2016; Wu et al. 2016). The leaf light use efficiency and water use efficiency may both vary as leaves age: young leaves and old leaves are less efficient than mature leaves, reflecting changes in photosynthetic capacity (Wilson et al. 2001; Wu et al. 2016). The timing of leaf flush and senescence can depend on the environment and on species; environmental stress, such as drought, can induce the process of senescence (Lim et al. 2007; Munné-Bosch and Alegre 2004).

In temperate evergreen broadleaved forests, such as eucalypt-dominated sclerophyll vegetation in Australia, precipitation can be seasonal or aseasonal; furthermore, day length and temperature vary significantly between winter and summer. GPP can be limited by frost during winter and by drought during summer. Atmospheric demand indicated by high vapor pressure deficit (D) and soil drought have different impacts on GPP, but they can interact to impact surface conductance (G_s) (Medlyn et al. 2011; Novick et al. 2016). In Australia's temperate eucalypt forests, canopy rejuvenation takes place in summer and is linked to heavy rainfall events (Duursma et al. 2016). However, since leaf flushing and shedding occur simultaneously in eucalypt canopies (Duursma et al. 2016; Pook 1984), the overall canopy volume can remain stable while the distribution of canopy volume changes with height (Griebel et al. 2015). Eucalypt forests in southeast Australia have been found to act as carbon sinks all year long, with greater uptake in summer (Hinko-Najera et al. 2017; van Gorsel et al. 2013). Although canopy characteristics are key to understanding ecosystem fluxes, their dynamics in Australian ecosystems can be particularly challenging to detect using standard vegetation indices (Moore et al. 2016). Nevertheless, the normalized difference vegetation index (NDVI) has successfully explained variability in photosynthetic capacity in Mediterranean, mulga and savanna ecosystems (Restrepo-Coupe et al. 2016).

80   The environmental and biotic controls on the seasonal dynamics of ecosystem fluxes in broadleaved
81   evergreen forests are still poorly understood. Our objective was to determine the seasonality of
82   ecosystem CO_2 and H_2O fluxes in a dry sclerophyll Eucalyptus forest; we evaluated the role of
83   environmental drivers (PPFD, T_a, SWC and D) and canopy dynamics (as measured with EVI, LAI,
84   litter fall and leaf age) in regulating the seasonal patterns of net ecosystem exchange (NEE), gross
85   primary productivity (GPP), ecosystem respiration (ER), evapotranspiration (ET) and surface
86   conductance (G_s) in an evergreen forest near Sydney, Australia. We also compared leaf-level to
87   ecosystem-level water and carbon exchange in response to drivers, in order to gain confidence in our
88   results and gain insights about the emergent properties from leaf to ecosystem scale. We hypothesised
89   that canopy phenology (LAI and leaf age) explains temporal variation in photosynthetic capacity (PC)
90   and G_s. We anticipated that the ecosystem would be a carbon sink all year long.

2. Material and methods

2.1 Site description

The field site is the Cumberland Plain (AU-Cum in Fluxnet) forest SuperSite (Resco de Dios et al. 2015) of the Australian Terrestrial Ecosystem Research Network (http://www.ozflux.org.au), located 50 km west of Sydney, Australia, at 19 m elevation, on a nearly flat floodplain of the Nepean-Hawkesbury River (latitude -33.61518; longitude 150.72362). Mean mid-afternoon (3 pm) temperature is 18 °C (max. 28.5 °C in January and min. 16.5 °C in July) and average precipitation is 801 mm year^{-1} (mean monthly max. is 96 mm in January, and min. is 42 mm in September). The soil is classified as a Kandosol and consists of a fine sandy loam A horizon (0-8 cm) over clay to clay loam subsoil (8-40 cm), with pH of 5 to 6 and up to 5% organic C in the top 10 cm (Karan et al. 2016). The flux tower is in a mature dry sclerophyll forest, with 140 Mg C ha^{-1} aboveground biomass and stand density of ~500 trees ha^{-1}. The stand hosts a large population of mistletoe (*Amyema miquelii*), which decreases in abundance with increasing distance to the flux tower. The canopy structure comprises three strata, and the predominant canopy tree species are *Eucalyptus moluccana* and *E. fibrosa*. While individual trees can exceed 25 m height, an airborne LiDAR survey from November 2015 indicates an average canopy height of ~24 m within a 300 m radius of the flux tower (supplement figure S1). The mid-canopy stratum (5-12 m) is dominated by *Melaleuca decora* and the understory is dominated by *Bursaria spinosa* with various shrubs, forbs, grasses and ferns present in lower abundance.

2.2 Environmental measurements

Air temperature (T_a) and relative humidity (RH) were measured using HMP45C and HMP155A (Vaisala, Vantaa, Finland) sensors at 7 m and 29 m heights, respectively. Vapour pressure deficit (D) was estimated from T_a and RH. Photosynthetic photon flux density above the canopy (PPFD, μmol m^{-2} s^{-1}) was measured using an LI190SB (Licor Inc., Lincoln NE, USA), and incoming and outgoing short and longwave radiation were measured using a CNR4 radiometer (Kipp & Zonen, Delft, Netherlands). Ancillary data were logged on CR1000 or CR3000 dataloggers (Campbell Scientific, Logan UT, USA) at 30 min intervals. Mixing ratios of CO_2 in air were also measured at 0.5 m, 1 m, 2 m, 3.5 m, 7 m, 12 m, 20 m, and 29 m above the soil surface using a LI840A Gas Analyzer (Licor Inc., Lincoln NE, USA); data from each height were logged on a CR1000 datalogger once every 30 minutes (1 minute air sampling per height).

Ground heat flux and soil moisture were averaged between two locations to represent the variable shading in the tower footprint. One location had a HFP01 heat flux plate and the other had a self-calibrating heat flux plate (HFP01SC) (Hukseflux, XJ Delft, Netherlands) installed at 8 cm below the soil surface. The heat flux plates were paired with a CS616 water content reflectometer (Campbell Scientific, Logan UT) installed horizontally at 5 cm below the soil surface and a TCAV averaging thermocouple (Campbell Scientific, Logan UT) installed with thermocouples at 2 cm and 6 cm below the soil surface for each pair. Another CS616 was installed vertically measured average soil water content from 7 to 37 cm (CS616). Rainfall was measured at an open area with a tipping bucket 2 km away from the study site.

2.3 Net ecosystem exchange

Continuous land-atmosphere exchange of CO_2 mass (net ecosystem exchange, NEE) was quantified from direct measurements of the different components of the theoretical mass balance of CO_2 in a control volume:

$$NEE = F_{CT} + F_{CS} \tag{1}$$

134 Where F_{CT} is the vertical turbulent exchange flux, and F_{CS} is the change in storage flux. Advection
135 fluxes are assumed negligible when atmospheric turbulence is sufficient (Aubinet et al. 2012;
136 Baldocchi et al. 1988), and when quality flags of stationarity and turbulence development test were
137 good (Foken et al. 2004). We used change-point detection of the friction velocity (u*) threshold (Barr
138 et al. 2013) to determine the turbulence threshold above which NEE (the sum of F_{CT} and F_{CS}) is
139 independent of u*. However, we found no clear dependence of NEE on u* hence no clear threshold
140 (Figure S2), so we used a threshold of 0.2 m s^{-1} to be conservative.

141 The calculation of each term, and the assumptions required for them to be representative of each half-
142 hour flux are detailed below.

2.4 Vertical turbulent flux (F_{CT})

144 The vertical turbulent fluxes of CO_2 (F_{CT}, µmol m^{-2} s^{-1}) and water (F_{WT}, mmol m^{-2} s^{-1}) were measured
145 using the eddy-covariance method (Baldocchi et al. 1988). Density (c) of CO_2 or water vapor (open-
146 path IRGA (LI-7500A, Licor Inc., Lincoln NE, USA)) and vertical wind speed (w) (CSAT 3D sonic
147 anemometer (Campbell Scientific, Logan UT, USA)) were measured at 10 Hz frequency at 29 m
148 above the ground, and logged on a CR-3000 datalogger (Campbell Scientific, Logan UT, USA).
149 Vertical turbulent fluxes were calculated from the 10 Hz data, using Eddy-Pro© software. Statistical
150 tests for raw data screening included spike count/removal, amplitude resolution, drop-outs, absolute
151 limits and skewness and kurtosis tests (Vickers and Mahrt 1997). Low and high frequency spectral
152 correction followed (Moncrieff et al. 2004), and (Moncrieff et al. 1997). The calculation allowed for
153 up to 10% of missing 10 Hz data. Fluxes were rotated into the natural wind coordinate system using
154 the double rotation method (Wilczak et al. 2001). Time lags between the sonic and IRGA were
155 compensated using covariance maximization, within a window of plausible time lags (Fan et al.
156 1990). We applied the block averaging method to calculate each half-hour average and fluctuation
157 relative to the average, to calculate the covariance (Gash and Culf 1996). Density fluctuations in the
158 air volume were corrected using the WPL terms (Webb et al. 1980). Each half-hourly flux was
159 associated with a quality flag (0: good quality, 1: keep for integrations, discard for empirical
160 relationships, 2: remove from the data); these flags accounted for stationarity tests and turbulence
161 development tests which are required for good turbulent flux measurements (Foken et al. 2004). In
162 our 4-year record, 51% of F_{CT} fluxes had a flag of 0, 32% had a flag of 1 and 17% had a flag of 2.
163 Although the tower height (29m) is rather close to the average canopy height (24m), cospectra
164 analysis showed good quality turbulent fluxes (the high frequency followed the -4/3 slope, thus we
165 did not find any indications of systematic dampening in the cospectra, see figure S3).

2.5 Storage flux (F_{CS})

167 The change in storage flux (F_{CS}, µmol m^{-2} s^{-1}) was measured using a CO_2 profiler system, such that
168 change of storage flux timestamp was the same as the turbulent flux timestamp. The change in storage
169 flux was calculated as (Aubinet et al. 2001):

$$F_{CS} = \frac{P_a}{R\,T_a} \int_0^h \frac{dC(z)}{dt} dz \qquad (2)$$

170 Where P_a is the atmospheric pressure (P_a), T_a is the temperature (K), R is the molar gas constant, and
171 C(z) is CO_2 (µmol m^{-3}) at the height z. CO_2 is measured in ppm and converted to µmol m^{-3} using ideal
172 gas law equation, where the air temperature and air pressure at each inlet is estimated from a linear
173 interpolation between sensors at the top of the tower (29m) and sensors at the bottom of the tower
174 (7m). As we only measure a limited number of heights, this equation becomes, in practice:

$$F_{CS} = \left(\frac{\Delta C}{\Delta t}\right)_{k=1} \times z_{k=1} + \sum_{k=2}^{n}\left\{\left[\left(\frac{\Delta C}{\Delta t}\right)_{k} + \left(\frac{\Delta C}{\Delta t}\right)_{k-1}\right] \times \frac{z_k - z_{k-1}}{2}\right\} \qquad (3)$$

175   Where C is CO_2 (µmol m^{-3}) and t is time (s) ($\Delta C/\Delta t$ is the variation of C over 30 minutes), z is the
176   height (m), k [1 to n = 8] represents each inlet. We flagged and replaced the storage flux with a one-
177   point approximation during profiler outages (25% of the 4-year record), using the change in CO_2 at 29
178   m height over 30 minutes as derived in EddyPro (Aubinet et al. 2001). These data were not used for
179   empirical relationships, but kept for annual sum calculations. Storage flux of water vapour was
180   assumed to be negligible. For visualisation of the diurnal course of storage flux and turbulent flux, see
181   Figure S4.

182   *2.6 Gap-filling of environmental variables and NEE separation into gross fluxes*
183   We used the PyFluxPro software for gap-filling climatic variables and fluxes, and for partitioning the
184   NEE into gross primary productivity (GPP) and ecosystem respiration (ER) (Isaac et al. 2017). We
185   only used observational data that passed the steady state and developed turbulence tests for gap-filling
186   and for partitioning (QC flags of 0 and 1; (Foken et al. 2004)). In brief, gaps in climate variables were
187   filled following the hierarchy of using variables provided from 1) automatic weather stations from the
188   closest weather station, 2) numerical weather prediction model outputs (ACCESS regional, 12.5 km
189   grid size provided by the Bureau of Meteorology) and lastly 3) monthly mean values from the site-
190   specific climatology. In a next step the continuous climate variables were used to fill all fluxes by
191   utilizing the embedded SOLO neural network with 25 nodes and 500 iterations on monthly windows.
192   We used 'Random Forest' (Breiman 2001) to determine and rank potential explanatory variables for
193   explaining latent heat flux (λE), sensible heat flux (H) and NEE. We then selected the five variables
194   with the highest feature importance for each flux and compared the gap-filling performance of the
195   neural network for each flux with the performance based on an educated guess of potential relevant
196   drivers. We selected the variable array with the highest Pearson correlation coefficient (r) and lowest
197   root mean square error (RMSE) for gap-filling in PyFluxPro, which identified net radiation (R_n), soil
198   water content (SWC), soil temperature (T_s), wind speed (w_s) and vapor pressure deficit (D) for λE (r =
199   0.93, RMSE = 32.0); down-welling shortwave radiation (F_{sd}), air temperature (T_a), T_s, w_s , SWC and
200   D for H (r = 0.97, RMSE = 23.1) and F_{sd}, D, T_a, T_s and SWC for NEE (r = 0.87, RMSE = 4.04). To
201   gap-fill ER, all nocturnal observational data (at night, we assume GPP = 0 so NEE = ER) that passed
202   all quality control checks and the u*-filter were modelled using T_s, T_a and SWC as drivers in SOLO
203   on the full dataset with 10 nodes and 500 iterations. Lastly, this gap-filled ER was used to infer GPP
204   as the result of NEE - ER.

205   *2.7 Flux footprint*
206   We analysed the footprint climatology of AU-Cum site according to (Kormann and Meixner 2001),
207   using the R-Package "FREddyPro' (Figure S5). We assumed that the ecosystem within the footprint
208   was homogeneous for the purpose of this study.

209   *2.8 Energy balance*
210   We evaluated the energy balance closure with the ratio of available energy (R_n – soil heat flux (G)) to
211   the sum of turbulent heat fluxes (λE + H). On a daily basis, the energy balance closure was 70%
212   (Figure S6), consistent with the well-known and common issue of a lack of closure (Foken 2008;
213   Foken et al. 2006; Wilson et al. 2002). We did not use the criteria that closure had to be met for the
214   reported fluxes.

2.9 Surface conductance

Surface conductance (G_s) was derived by inverting the Penman-Monteith equation (Monteith 1965):

$$G_s = \frac{\gamma \, \lambda E \, g_a}{\Delta \, R_n + \rho \, C_p \, D \, g_a - \lambda E \, (\Delta + \gamma)} \tag{4}$$

Where γ is the temperature dependent psychrometric constant (kPa K^{-1}), λE is the latent heat flux (W m^{-2}), Δ is the temperature dependent slope of the saturation-vapor pressure curve (kPa K^{-1}), R_n is net radiation (W m^{-2}), ρ is the dry air density (kg m^{-3}), D is vapor pressure deficit (kPa), C_p is the specific heat of air (J kg^{-1} K^{-1}), and g_a is the bulk aerodynamic conductance, formulated as an empirical relation of mean horizontal wind speed (U, m s^{-1}) and friction velocity (u*, m s^{-1}) (Thom 1972):

$$g_a = \frac{1}{\frac{U}{u^{*2}} + 6.2 \, u^{*-0.67}} \tag{5}$$

In the analysis for G_s, we were interested in transpiration (T) rather than evaporation (E), so we excluded data if precipitation exceeded 1 mm in the past 2 days, 0.5 mm in the past 24 hours, and 0.2 mm in the past 12 hours (Knauer et al. 2015). We assumed that evaporation (E) is negligible using these criteria (Knauer et al. 2017), which excluded 40% of the data.

2.11 Dynamics of canopy phenology (leaf area index, litter and leaf production) and photosynthetic capacity

We evaluated the dynamics of canopy leaf area index (LAI) by measuring canopy light transmittance with three under-canopy PPFD sensors and one above canopy PPFD sensor LI190SB (Licor Inc., Lincoln NE, USA) following the methods presented in (Duursma et al. 2016). Although we use the term LAI, this estimate does include non-leaf surface area (stems, branches). We collected litterfall (L_f, g m^2 month^{-1}) in the tower footprint approximately once per month, from nine litter traps (0.14 m^{-2} ground area) located near the understory PPFD sensors. We estimated specific leaf area (SLA) of eucalyptus and mistletoe leaves by sampling approximately 50 fresh leaves of each, in June 2017 (SLA = 56.4 cm^2 g^{-1} for eucalyptus, 40.3 cm^2 g^{-1} for mistletoe). For each month, we partitioned the litter into eucalyptus leaves, mistletoe leaves, and other (mostly woody) components. We used this SLA to estimate leaf litter production (L_p) in m^2 m^{-2} month^{-1} of eucalyptus, mistletoe, and total as the sum of both. Then, we estimated leaf growth (L_g, m^2 month^{-2}) as the sum of the net change in LAI (ΔL) and L_p. Photosynthetic capacity (PC) is defined as median GPP when PPFD is 800-1200 µmol m^{-2} s^{-1} and D is 1.0 to 1.5 kPa.

2.12 Analysis of light-response of NEE

We evaluated the light response of NEE using a saturating exponential function (Eq. 5) to test whether parameters varied between seasons (Aubinet et al. 2001; Lindroth et al. 2008; Mitscherlich 1909).

$$NEE = -(NEE_{sat} + R_d) \left(1 - \exp\left[\frac{-\alpha \, PPFD}{NEE_{sat} + R_d} \right] \right) + R_d \tag{7}$$

where the parameter R_d is the intercept, or NEE in the absence of light, often called dark respiration; NEE_{sat} is NEE at light saturation and α is the initial slope of the curve, expressed in µmol CO$_2$ µmol photon^{-1} and representing light use efficiency when photosynthetic photon flux density (PPFD) is close to 0. We only used daytime quality checked NEE data to fit the model (qc = 0; (Foken et al.

248   2004), LI-7500 signal strength = max, all inlets of profiler system data available and $u* > 0.2$ m s^{-1}),
249   see Figure S7.

250   *2.13 Leaf gas exchange spot measurements*
251   We used previously published data of spot leaf gas exchange measurements in a nearby site for
252   comparison with ecosystem fluxes (Gimeno et al. 2016).

253   *2.14 Remotely sensed land surface greenness*
254   Normalized difference vegetation index (NDVI) and Enhanced Vegetation Index (EVI) values were
255   derived from the MODIS Terra Vegetation Indices 16-Day L3 Global 250m product (MOD13Q1),
256   which uses atmospherically corrected surface reflectance masked for water, clouds, heavy aerosols,
257   and cloud shadows (Didan 2015). At 250m spatial resolution, the pixel containing Cumberland Plain
258   was assumed to be representative for the footprint and values of that pixel between 1.1.2014 and
259   31.12.2017 were extracted.

3 Results

3.1 Seasonality of environmental drivers and leaf area index

Climatic conditions were favorable for growth at the site year-round. The monthly average of daily maximum air temperature was 16.3 °C during the coldest month (July 2015), and the lowest monthly average of daily maximum PPFD was 878 µmol m^{-2} s^{-1} in the winter (June 2015; Figure 1c). Although less rainfall occurred during winter months compared to summer months, precipitation occurred throughout the year (Figure 1b). Soil volumetric water content (SWC) in the shallow (0-8 cm) layer was about 10% except immediately following rain events (Figure 1b). In contrast, SWC in the clay layer (8 -38cm) remained above 30% for the duration of the study (data not shown). Monthly average of daily maximum air temperature ranged from 16.3 °C in July 2015 to 32.7 °C in January 2017; monthly average of daily maximum D ranged from 0.9 kPa in June 2015 to 3.4 kPa in January 2017 (Figure 1c). For visualisation of seasonal and diurnal trends of radiation, air temperature, D and SWC, see supplement Figure S8.

Canopy leaf area index varied between 0.7 (in December 2014) and 1.15 m^2 m^{-2} (in March 2016 and June 2017) (Figure 1d). LAI followed a distinct pattern: it peaked in late summer (around February), and then continuously decreased until the new leaves emerged the following year. A late leaf flush was observed in 2017 (May). Litter production also peaked in summer, before and during the leaf flush, and was lower in winter (Figure 1d). EVI followed the time dynamic of LAI.

3.2 Seasonality of carbon and water fluxes

Contrary to expectations, the ecosystem was always a sink for carbon in winter (-146 g C m^{-2} on average, with a standard deviation of 22 g C m^{-2}), and usually a carbon source or close to neutral in summer (+ 44 g C m^{-2} on average, with a standard deviation of 43 g C m^{-2}) (Table 1). On average, summer GPP was lower – i.e. more uptake (-400 ± 97 g C m^{-2}) compared to winter GPP (-282 ± 41 g C m^{-2}) (Table 1), that is a difference of ~ 118 g C m^{-2}. However, average summer ER was much higher (444 ± 56 g C m^{-2}) compared to winter ER (159 ± 35 g C m^{-2}) (Table 1), a difference of ~ 285 g C m^{-2}. The summer vs. winter ER difference was more than double the GPP difference; thus, ER had a relatively larger effect over the seasonality of NEE.

3.3 Diurnal trend of CO$_2$ flux and drivers in winter and summer

The diurnal pattern of NEE in clear-sky conditions differed between summer and winter (Figure 2). Relatively speaking, diurnal NEE was more symmetric in the winter than in summer. That is, morning and afternoon NEE pattern resembled a mirror image and total integrated morning NEE was similar to integrated afternoon NEE during the winter, but strong hysteresis occurred in the summer (Figure 2). This pattern also translated into hysteresis in the NEE light response curve in summer, but to a lesser degree in winter (Figure 3).

3.4 Analysis of NEE light response curve

The parameters of the NEE light response in summer and winter are shown in Figure 4 (see methods, Eq. 5). The initial slope of NEE with light (α) showed no clear dependence on T_{soil} in winter but exhibited sensitivity during summer, dropping precipitously at soil temperature above 23 °C (Figure 4a). α increased with SWC in winter and summer by a factor of 1.5 (Figure 4b). In both winter and summer α decreased with D (D > 1 kPa) and in a similar fashion, approaching a saturating value of 0.01 (µmol µmol^{-1}) at a D of about 2 kPa (Figure 4c). The fitted NEE at saturating light (NEE$_{sat}$) was not related to T_{soil} in winter but decreased with increasing T_{soil} in summer (Figure 4d). NEE$_{sat}$ was higher in winter than in summer for a given SWC. The relationship with D was more complicated, tending to increase with D in winter, but decreasing with increased D in summer, dropping from 9 to

304 3 (μmol m^{-2} s^{-1}) as D increased from 1 to 4 kPa. R_d was significantly higher in summer than winter
305 across all conditions of T_{soil}, SWC and D (Figure 4g, h, i). R_d increased with T_{soil} in winter and less so
306 in summer. In winter, R_d increased up to SWC of 11%; in summer, R_d was more sensitive to SWC,
307 doubling from a rate of ~ 4 to ~ 8 μmol m^{-2} s^{-1} as SWC increased from about 8 to 20%.

308 *3.5 Atmospheric demand and soil drought control on GPP, ET, G_s and WUE*
309 We evaluated the effect of SWC and vapour pressure deficit (D) on GPP, ET, water use efficiency
310 (WUE) and surface conductance (G_s) under high radiation ("light-saturated"; PPFD > 1000 μmol m^{-2}
311 s^{-1}), after filtering periods following rain events in order to minimise the contribution of evaporation
312 to ET (see Methods) (Figure 5). In summer, light-saturated GPP decreased above D ~ 1.3 kPa, but in
313 winter, GPP did not vary with D. In summer and in winter, GPP increased with SWC (Figure 5a).
314 This is consistent with Figure 4, where R_d and NEE_{sat} both increased with SWC. In summer, light-
315 saturated ET increased with D up to ~1.3 kPa, above which it reached a plateau. In winter, ET kept
316 increasing with D, as D rarely exceeded 2 kPa. In both seasons, ET increased with SWC (Figure 5b).
317 Surface conductance decreased with D and SWC especially in summer, indicating strong stomatal
318 regulation (Figure 5d). WUE decreased with increasing D in summer and in winter, because ET
319 increased but -GPP declined (Figure 5c).

320 We compared these ecosystem-scale results to the equivalent at the leaf-scale, which are net
321 photosynthesis at light saturation A_{max} (PPFD ~ 1800 μmol m^{-2} s^{-1}), leaf transpiration T, leaf water use
322 efficiency, and stomatal conductance g_s (Figure 5, black lines). These leaf level measurements are
323 expressed on a leaf-area basis, as compared to ground area for ecosystem scale. We observed that
324 A_{max}, T and g_s were more sensitive to D than corresponding ecosystem-scale responses. A_{max} was
325 much higher than GPP_{max} at D ~ 1 kPa, while g_s was comparable in magnitude to G_s in the same
326 condition. Leaf transpiration peaked around D = 1.2 kPa, while ET plateaued. Leaf water use
327 efficiency was overall higher than ecosystem WUE.

328 *3.6 Canopy phenology control of GPP*
329 Monthly average photosynthetic capacity (PC) varied by a factor of ~2 across the study period,
330 ranging from 8.4 μmol m^{-2} s^{-1} before the leaf flush in November 2014 to 15 μmol m^{-2} s^{-1} after the leaf
331 flush occurred in March 2016. We expected that PC could be predicted by LAI, EVI and G_s. Leaf area
332 index (LAI) and photosynthetic capacity (PC) were significantly correlated; the slope was
333 significantly different from zero ($r^2 = 0.29$, $p < 0.005$, PC = 8.3 LAI + 3.0, Figure 6). EVI was even
334 more significantly correlated with PC ($r^2 = 0.46$, $p < 0.005$, PC = 52 EVI – 5.3, Figure 6). $G_{s,max}$ was
335 significantly correlated with PC ($r^2 = 0.2$, $p < 0.005$, PC = 9 $G_{s,max}$ + 9) and LAI ($r^2 = 0.30$, $p < 0.005$,
336 $G_{s,max} = 0.45$ LAI – 0.18) and with EVI ($r^2 = 0.29$, $p < 0.005$, $G_{s,max} = 2.3$ EVI – 0.45). The
337 correlations with NDVI were less significant than with EVI (see figure S9).

4 Discussion

We measured four consecutive years of carbon, water and energy fluxes in a native evergreen broadleaf eucalyptus forest, including canopy dynamics and environmental drivers (photosynthetically active radiation, air and soil temperature, precipitation, soil water content, and atmospheric demand). We hypothesised that the Cumberland Plain forest would be a carbon sink all year-round, similar to other eucalypt forests (Beringer et al. 2016; Hinko-Najera et al. 2017; Keith et al. 2012). We also hypothesised higher net carbon uptake during summer, due to warmer temperatures, higher light and longer day length contributing to higher photosynthesis, compared to winter. However, the site was a net source of carbon during summer, and a net sink of carbon during winter.

The seasonal pattern of NEE was driven mostly by ER, as the seasonal amplitude of ER was larger than the seasonal amplitude of GPP. The seasonality of ER may be explained by the positive effects of higher temperatures on the rates of autotrophic respiration (Tjoelker et al. 2001), and on the activity of microbes to increase soil organic matter decomposition (Lloyd and Taylor 1994); low soil moisture in the shallow layers sometimes limited decomposition (January and February 2014, January and December 2015, February and December 2017, see Figure 1), but often regular rainfall maintained adequate soil moisture. The relatively low seasonality of GPP may be partly explained by lower photosynthetic capacity in early summer (before January) when LAI was at its lowest, and the leaves have reached maximum age because new leaves have not yet emerged. The ER-driven seasonality of NEE is in sharp contrast with cold temperate forests where GPP drives the seasonality of NEE. ER-driven NEE seasonality was also observed in an Asian tropical rain forest, as ER was higher than GPP in the rainy season leading to net ecosystem carbon loss, while in the dry season, ecosystem carbon uptake was positive (Zhang et al. 2010). This pattern was also observed in an Amazon tropical forest (Saleska et al. 2003).

A strong morning-afternoon hysteresis of NEE response to PPFD occurred in summer, and less so in winter (Figure 3). In winter, low D and moderately warm daytime air temperatures and high PPFD were sufficient to maintain high photosynthesis rates throughout most of the day (Figure 1). In summer, two possible explanations of the diurnal hysteresis of NEE are (1) ER is greater in the afternoon compared to morning or (2) GPP is lower in the afternoon compared to morning. Explanation (1) is plausible, as temperature drives autotrophic and heterotrophic respiration; however, it is unlikely to explain the hysteresis magnitude which is higher in summer compared to winter. Explanation (2) could arise from lower afternoon stomatal conductance or lower photosynthetic capacity (e.g. the maximum rate of carboxylation (Vcmax) decreases at high T_a), or a combination of both or even circadian regulation (Jones et al. 1998; Resco de Dios et al. 2015). An analysis of surface conductance showed strong stomatal regulation (Figure 2, Figure 3, Figure 5), induced by high atmospheric demand and high air temperature (Duursma et al. 2014), limiting photosynthesis during the afternoon of warm months (see Figure S10). These diurnal patterns of NEE, GPP and ER play a strong role in regulating the seasonal carbon cycling dynamics in this ecosystem. A wavelet coherence analysis between D and GPP showed strong coherence at seasonal time scale (periods of three months), see figure S11.

We observed comparable responses of leaf-level and ecosystem-level gas exchange to environmental drivers (Figure 5). The larger magnitude of A_{max} than GPP at high D may be explained by the proportion of shaded leaves in the ecosystem. The similar magnitude for G_s and g_s was also expected, as LAI is close to 1 and R_n is not a driver for stomatal conductance. The peaked pattern of T versus D, as opposite to saturating pattern of ET, may be explained by (1) the contribution of soil evaporation to

383 ET or (2) the presence of mistletoe, known for not regulating their stomata (Griebel et al. 2017). The
384 higher magnitude of leaf water use efficiency results from the combination of higher A_{max} and similar
385 or lower leaf transpiration compared to ET. Furthermore, we compared leaf level g_1 and ecosystem
386 level G_1, using the optimal stomatal conductance model (Medlyn et al. 2011): G_1 was lower than g_1
387 $(1.6 \pm 0.06$ for G_1, 4.4 ± 0.2 for g_1, see figure S12).

388 Our study demonstrated that canopy dynamics (specifically, LAI in our study) play an important role
389 in regulating seasonal variations in GPP even in evergreen forests. Similar observations emerged from
390 a tropical forest, where leaf area index and leaf age explained the seasonal variability of GPP (Wilson
391 et al. 2001; Wu et al. 2016), as the photosynthetic capacity (PC, the maximum rate of GPP in optimal
392 environmental condition) varied with leaf age. In Australian woodlands, PC (A_{max}) of leaves was also
393 found to decrease with leaf age: A_{max} declined by 30% on average between young and old leaves, for
394 10 different species (Reich et al. 2009). In the Cumberland Plain forest, periods with high LAI co-
395 occur with mature, efficient leaves, and periods with low LAI co-occur with old, less efficient leaves.
396 LAI was correlated with PC, which was probably the result of both a greater number of leaves and
397 more efficient leaves. Remotely sensed vegetation indices such as EVI or NDVI assess whether the
398 target being observed contains live green vegetation. In Australia, NDVI and EVI were good
399 predictors of photosynthetic capacity in savanna, mulga and Mediterranean-mallee ecosystems
400 (Restrepo-Coupe et al. 2016). For our site, EVI was a good predictor of PC, which was surprising as
401 satellite-derived LAI values have been found to be typically inaccurate in open forests and forests in
402 southeast Australia (Hill et al. 2006). NDVI was a poor predictor of PC (see figure S9).

403 In a global study, it was shown that mean annual NEE decreased with increasing dryness index
404 (PET/P) in sites located below 45° N latitude (Yi et al. 2010). It has also been shown that *Eucalyptus*
405 grow more slowly in warm environments (Prior and Bowman 2014). At our site, and in a previous
406 study in eucalyptus forest (van Gorsel et al. 2013), GPP decreased with D above a threshold of ~ 1.3
407 kPa. Our results indicate that surface conductance (G_s) decreased above that threshold, suggesting that
408 the decrease in GPP is caused by stomatal regulation. As D correlates with air temperature, it is
409 difficult to distinguish the relative contribution of D and T_a to the decrease of G_s, but they are thought
410 to both impact G_s (Duursma et al. 2014). Cumberland Plain has the highest mean annual temperature
411 and the highest dryness index among the four eucalyptus forest eddy-covariance sites in south-east
412 Australia (Beringer et al. 2016), which could explain its strong sensitivity to D and hence its unique
413 seasonality.

5 Conclusions

The Cumberland Plain forest was a net C source in summer and a net C sink in winter, in contrast to other Australian eucalypt forests which were net C sinks year-round. ER drove NEE seasonality, as the seasonal amplitude of ER was greater than GPP. ER was high in the warmer, wetter months of summer, when environmental conditions supported high autotrophic respiration and heterotrophic decomposition. Meanwhile, GPP was limited by lower LAI and probably older leaves in early summer, and by high D which limited G_s throughout the summer. Despite being evergreen, there was significant temporal variation in LAI, which was correlated with monthly photosynthetic capacity and monthly surface conductance. Understanding LAI dynamics and its response to precipitation regimes will play a key-role in climate change feedback.

Code and data availability

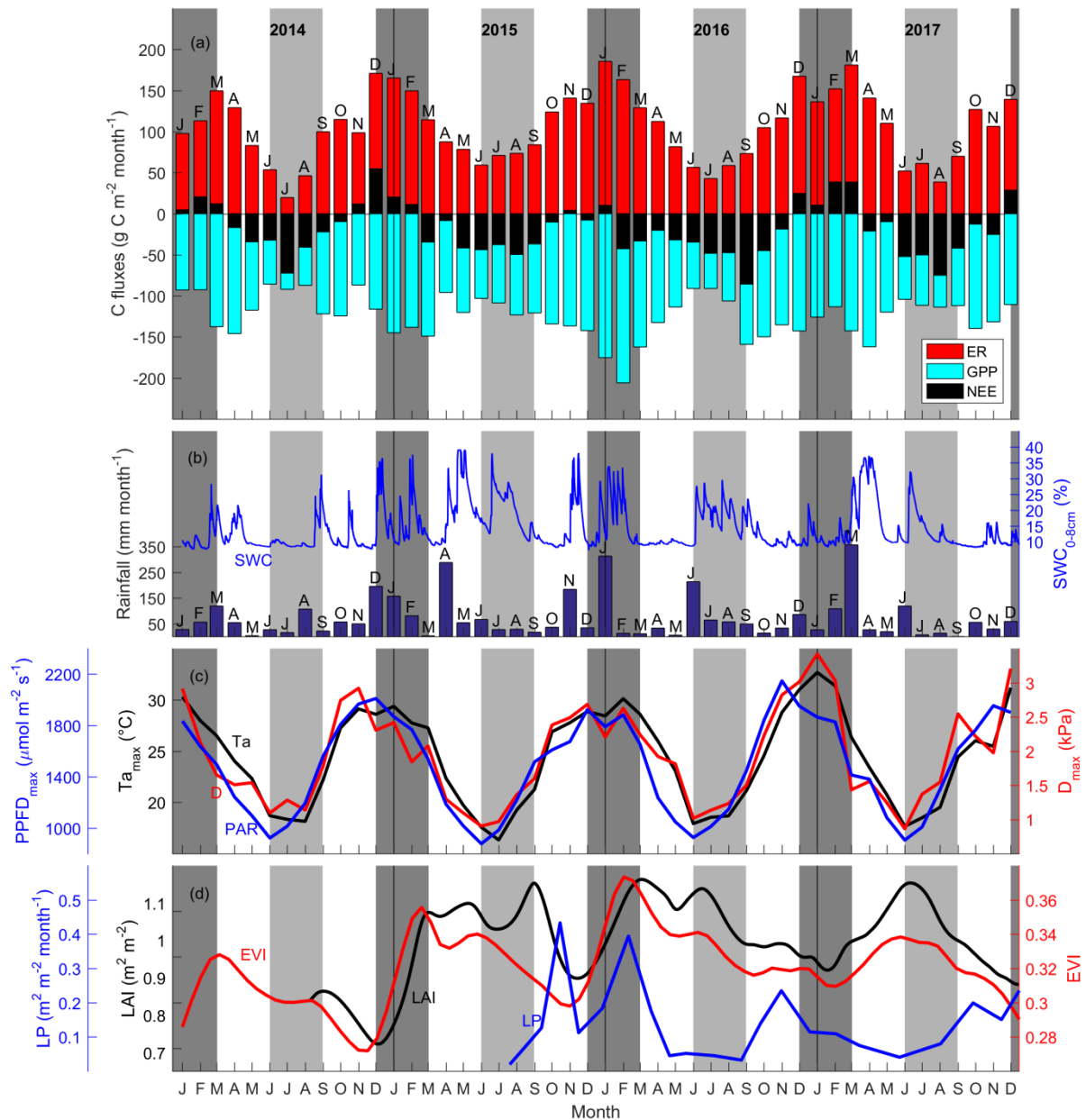All the datasets and scripts used in this manuscript can be downloaded at:

http://doi.org/10.5281/zenodo.1219977

Author contribution

DT, VRD, EP, AAR conceived the project; CVMB, CM, EP, AAR, AG, MMB, DM collected the data and assured the maintenance of the experiment; AAR, AG, DM, CAW, EP, PI, VRD, analysed the data; AAR and EP wrote the manuscript with input from all other authors.

The authors declare that they have no conflict of interest.

437

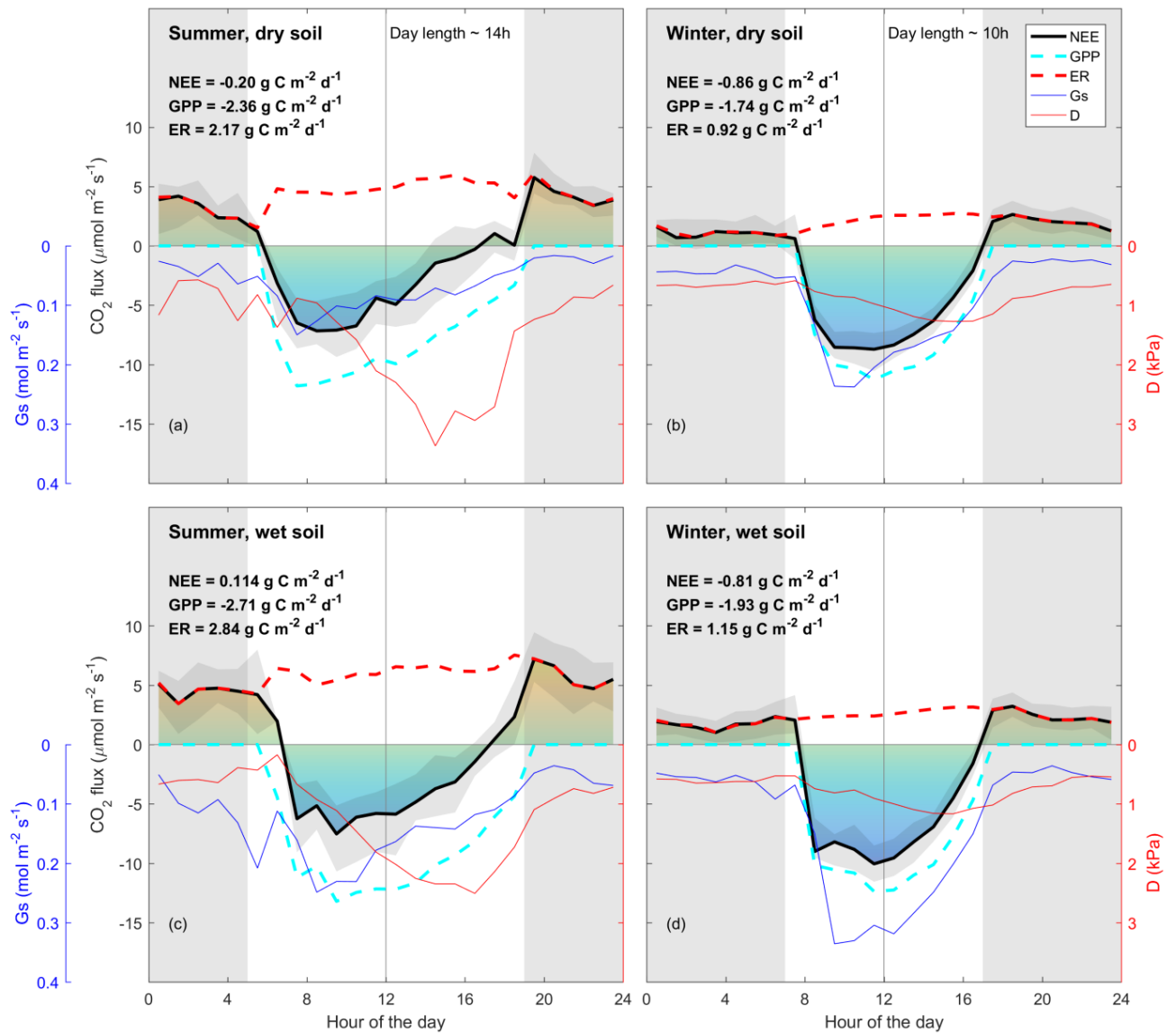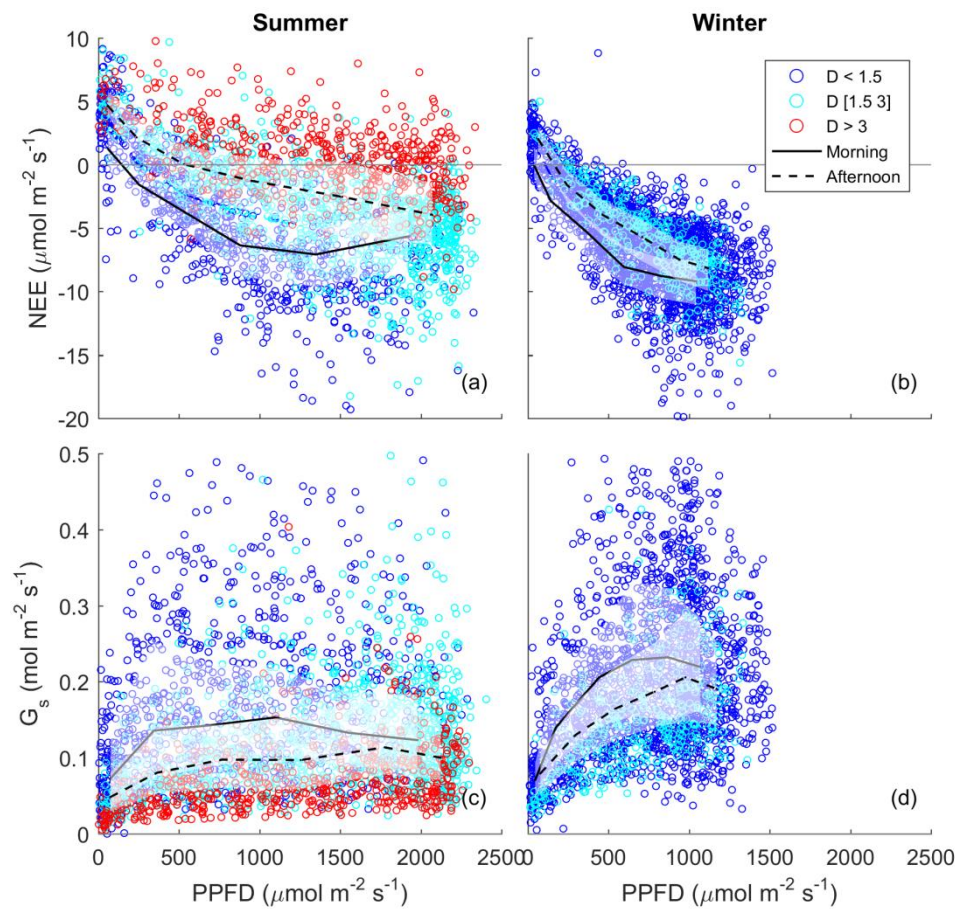438 **Figure 1** a) Time series of monthly carbon flux (net ecosystem exchange (NEE), ecosystem respiration (ER) and gross
439 primary productivity (GPP), g C m^{-2} month^{-1}) (negative indicates ecosystem uptake); b) rainfall, mm month^{-1}; soil water
440 content from 0 to 8 cm (SWC$_{0-8cm}$, %); c) average of daily maximum for each month photosynthetically active radiation
441 (PPFD$_{max}$, µmol m^{-2} s^{-1}), air temperature (Ta$_{max}$, °C) and vapour pressure deficit (D$_{max}$, kPa). d) Canopy dynamics trends:
442 enhanced vegetation index (EVI, unitless); leaf area index (LAI, m^2 m^{-2}) and litter production (L$_P$, m^2 m^{-2} month^{-1}). Shaded
443 areas shows summer (dark grey) and winter (light grey). Note Ta$_{max}$ and PPFD$_{max}$ remained above 15 °C and 800 µmol m^{-2} s^{-}
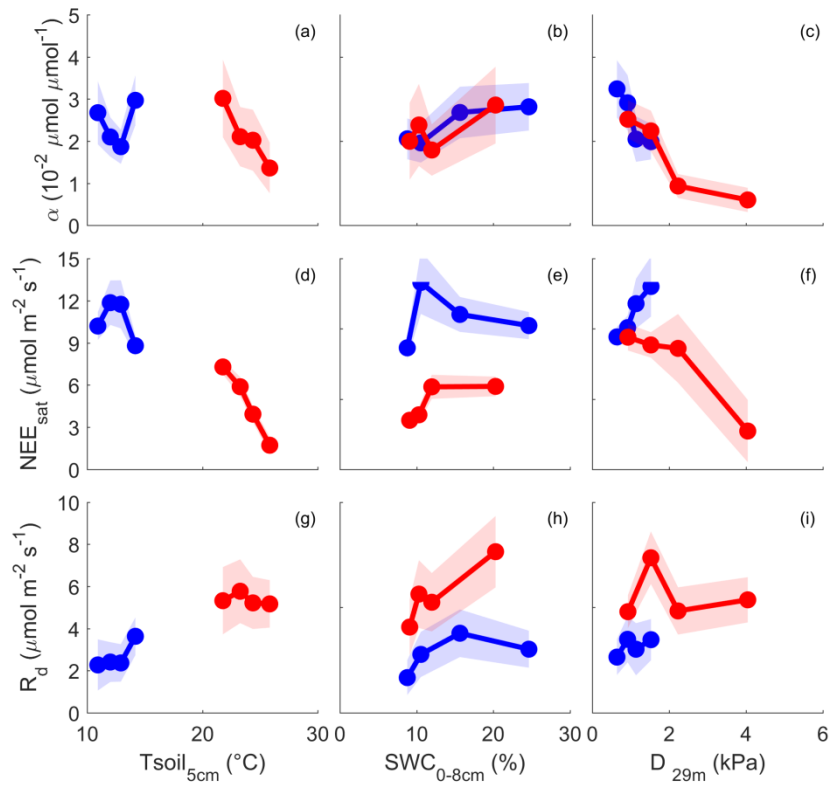444 ^{1}.

14

Figure 2 Diurnal trend (line: median and shade: quartile) of clear-sky measured net ecosystem exchange (NEE, thick black line, $\mu mol\ m^{-2}\ s^{-1}$); estimated daytime ecosystem respiration (ER, inferred from a neural network fitted on nighttime NEE, thick dotted red line, $\mu mol\ m^{-2}\ s^{-1}$); estimated gross primary productivity (GPP, inferred as NEE – estimated daytime ER, thick dotted cyan line, $\mu mol\ m^{-2}\ s^{-1}$); measured vapour pressure deficit (D, thin red line, kPa); and estimated surface conductance (G_s, inferred from Penman-Monteith, blue line, $mmol\ m^{-2}\ s^{-1}$). Grey shade shows night-time (sunset to sunrise). NEE, GPP and ER number are calculated by integrating the diurnal fluxes as shown in the figure. "Wet" and "dry" soil is defined as below or above the median of soil water content during summer or winter. Summer is December through February. Winter is June through August, as defined by the Sydney bureau of meteorology. Colours under NEE rate are shown for visualisation. Note that there is an asymmetry between morning and afternoon NEE in summer, less so in winter. Note that ecosystem respiration (nighttime NEE) is enhanced by SWC in summer, less so in winter. Data used in this figure correspond to clear-sky half-hour values, where high quality measured data for NEE were available.
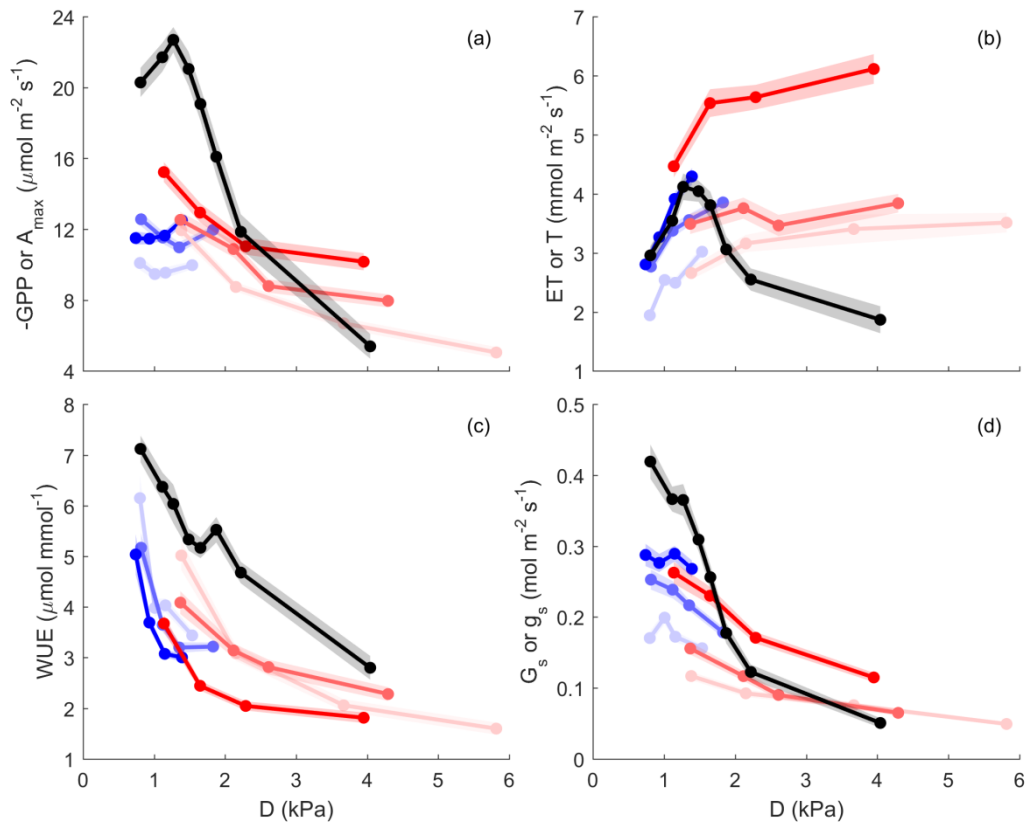
457

Figure 3 Half-hourly measured NEE vs. PPFD, coloured by D (blue, D < 1.5 kPa, cyan: D [1.5-3] kPa, red: D > 3 kPa) for
(a) summer, and (b) winter periods. Raw data are binned by light levels to show median (lines) and quartiles (white shades)
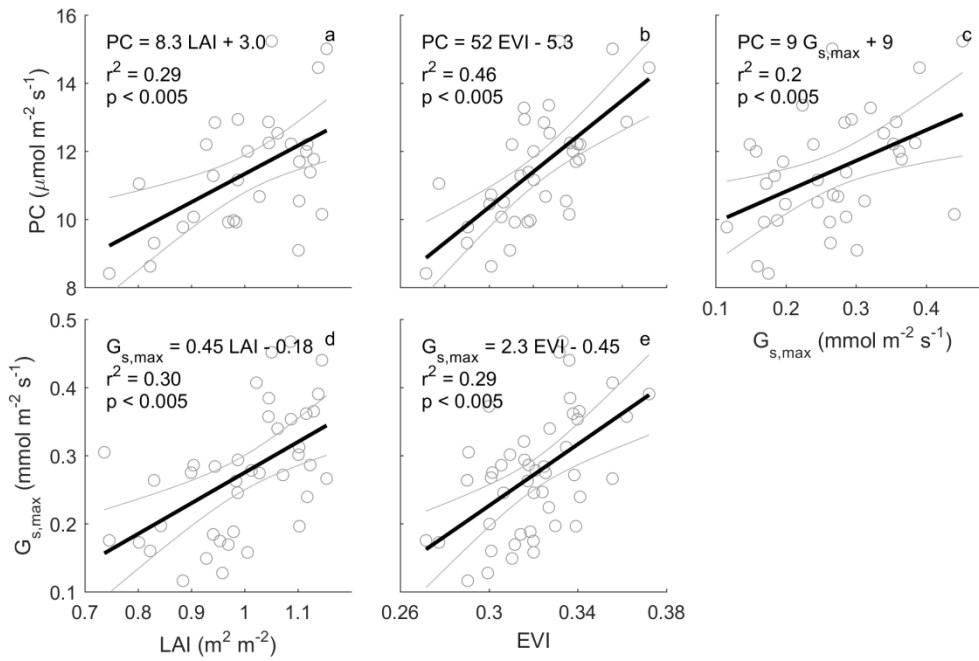for morning (continuous lines) and afternoon (dotted lines) hours separately.

461

Figure 4 NEE μmol m^{-2} s^{-1} light response parameters, calculated for different bins of climatic drivers (soil temperature (T$_{soil}$, °C) at 5cm depth, soil water content (SWC, %) from 0 cm to 8 cm depth, and atmospheric demand (D, kPa) at 29 m height), only raw, qc filtered daytime data is used. Light response curve was fitted using Mitscherlich equation (see methods), α is the initial slope, near PPFD = 0 (μmol μmol^{-1}), NEE$_{sat}$ μmol m^{-2} s^{-1} is NEE at light saturation, and R$_d$ μmol m^{-2} s^{-1} is the dark respiration (NEE when PPFD = 0). Blue indicates winter months, Red indicates summer months. Dots are parameters value for each quartile of driver, plotted at x = median of driver for each bin. Shading is 95% confidence interval of the parameter fit.

469

Figure 5 Gross primary productivity or net assimilation (GPP or Amax, µmol m^{-2} [ground or leaf] s^{-1}), evapotranspiration or leaf transpiration (ET or T, mmol m^{-2} [ground or leaf] s^{-1}), water use efficiency (WUE = GPP/ET or A$_{max}$/T, µmol mmol^{-1}) and surface conductance or leaf conductance (G$_s$ or g$_s$, mmol m^{-2} s^{-1}) vs. vapour pressure deficit (D). Leaf level is shown in black, ecosystem scale is shown in color; summer (red) and winter (blue), at saturated PPFD (>1000 µmol m^{-2} s^{-1}). D is binned into 4 quartiles for ecosystem and 8 for leaf; Y is mean value for each D bins, plotted at the median of D bin. Shaded area indicates the standard error of the mean. The three color intensity show SWC quantiles (SWC < 0.33, SWC [0.33-0.67] and SWC [0.67-1.00] shown in decreasing color intensity).

18

477

478 **Figure 6** Relationships between monthly photosynthetic capacity (PC, µmol m^{-2} s^{-1}), leaf area index (LAI, m^2 m^{-2}),
479 enhanced vegetation index (EVI), and maximum surface conductance (G$_{s,max}$). Monthly PC and monthly G$_{s,max}$ are calculated
480 as the median of half-hourly GPP and half-hourly G$_s$ when PPFD [800-1200 µmol m^{-2} s^{-1}] and D [1-1.5 kPa]; rain events are
481 filtered for G$_{s,max}$ estimation, to minimise evaporation contribution to evapotranspiration (see methods). Monthly LAI is
482 calculated as mean of LAI smoothed by a spline. Thick black line shows a linear regression. For PC calculation, GPP data is
483 only used when quality-checked NEE is available (GPP = NEE measured − ER estimated by a neural network, see method).

484 **Table 1** Annual precipitation (P, mm y^{-1}), evapotranspiration (ET, mm y^{-1}), air temperature T$_a$ (°C), net ecosystem exchange
485 (NEE, g C m^{-2} y^{-1}), gross ecosystem production (GPP, g C m^{-2} y^{-1}) and ecosystem respiration (ER, g C m^{-2} y^{-1}) for the four
486 year study period.

Period	P (mm y^{-1})	ET (mm y^{-1})	T$_a$ (°C)	NEE (g C m^{-2} y^{-1})	GPP (g C m^{-2} y^{-1})	ER (g C m^{-2} y^{-1})
2014 all	**733**	**797**	**18**	**-124**	**-1301**	**1177**
Winter	149	142	13	-145	-265	120
Spring	129	189	19	-20	-333	313
Summer	279	275	23	80	-302	382
Autumn	176	190	19	-39	-401	362
2015 all	**978**	**938**	**18**	**-234**	**-1517**	**1283**
Winter	122	160	12	-131	-335	204
Spring	237	223	19	-43	-392	349
Summer	273	318	23	24	-426	449
Autumn	345	238	18	-84	-365	280
2016 all	**893**	**852**	**19**	**-372**	**-1664**	**1292**
Winter	335	164	13	-130	-288	158
Spring	96	207	19	-149	-444	295
Summer	412	311	24	-8	-524	516
Autumn	50	171	20	-85	-408	323
2017 all	**821**	**798**	**19**	**-171**	**-1486**	**1315**
Winter	139	148	13	-177	-329	152
Spring	85	178	19	-80	-383	303
Summer	194	236	25	78	-350	428
Autumn	403	237	18	8	-424	432

487

References

Aubinet, M., T. Vesala, and D. Papale, 2012: *Eddy Covariance A Practical Guide to Measurement and Data Analysis.* Springer.

Aubinet, M., B. Chermanne, M. Vandenhaute, B. Longdoz, M. Yernaux, and E. Laitat, 2001: Long term carbon dioxide exchange above a mixed forest in the Belgian Ardennes. *Agricultural and Forest Meteorology*, **108,** 293-315.

Baldocchi, D., Y. Ryu, and T. Keenan, 2016: Terrestrial Carbon Cycle Variability. *F1000Research*, **5**.

Baldocchi, D. D., B. B. Hicks, and T. P. Meyers, 1988: MEASURING BIOSPHERE-ATMOSPHERE EXCHANGES OF BIOLOGICALLY RELATED GASES WITH MICROMETEOROLOGICAL METHODS. *Ecology*, **69,** 1331-1340.

Barr, A., and Coauthors, 2013: Use of change-point detection for friction–velocity threshold evaluation in eddy-covariance studies. *Agricultural and Forest Meteorology*, **171,** 31-45.

Beringer, J., and Coauthors, 2016: An introduction to the Australian and New Zealand flux tower network - OzFlux. *Biogeosciences*, **13,** 5895-5916.

Breiman, L., 2001: Random forests. *Machine learning*, **45,** 5-32.

Didan, K., 2015: MOD13Q1 MODIS/Terra Vegetation Indices 16-Day L3 Global 250 m SIN Grid V006. *NASA EOSDIS Land Processes DAAC*.

Dixon, R. K., S. Brown, R. e. a. Houghton, A. Solomon, M. Trexler, and J. Wisniewski, 1994: Carbon pools and flux of global forest ecosystems. *Science(Washington)*, **263,** 185-189.

Duursma, R. A., T. E. Gimeno, M. M. Boer, K. Y. Crous, M. G. Tjoelker, and D. S. Ellsworth, 2016: Canopy leaf area of a mature evergreen Eucalyptus woodland does not respond to elevated atmospheric CO2 but tracks water availability. *Global Change Biology*, **22,** 1666-1676.

Duursma, R. A., and Coauthors, 2014: The peaked response of transpiration rate to vapour pressure deficit in field conditions can be explained by the temperature optimum of photosynthesis. *Agricultural and Forest Meteorology*, **189,** 2-10.

Fan, S.-M., S. C. Wofsy, P. S. Bakwin, D. J. Jacob, and D. R. Fitzjarrald, 1990: Atmosphere-biosphere exchange of CO 2 and O 3 in the central Amazon forest.

Foken, T., 2008: The energy balance closure problem: an overview. *Ecological Applications*, **18,** 1351-1367.

Foken, T., F. Wimmer, M. Mauder, C. Thomas, and C. Liebethal, 2006: Some aspects of the energy balance closure problem. *Atmospheric Chemistry and Physics*, **6,** 4395-4402.

Foken, T., M. Gockede, M. Mauder, L. Mahrt, B. Amiro, and W. Munger, 2004: Post-field data quality control. *Handbook of Micrometeorology: A Guide for Surface Flux Measurement and Analysis*, **29,** 181-208.

Gash, J., and A. Culf, 1996: Applying a linear detrend to eddy correlation data in realtime. *Boundary-Layer Meteorology*, **79,** 301-306.

Gimeno, T. E., K. Y. Crous, J. Cooke, A. P. O'Grady, A. Ósvaldsson, B. E. Medlyn, and D. S. Ellsworth, 2016: Conserved stomatal behaviour under elevated CO2 and varying water availability in a mature woodland. *Functional Ecology*, **30,** 700-709.

527   Graham, E. A., S. S. Mulkey, K. Kitajima, N. G. Phillips, and S. J. Wright, 2003: Cloud cover limits
528   net CO2 uptake and growth of a rainforest tree during tropical rainy seasons. *Proceedings of the*
529   *National Academy of Sciences*, **100,** 572-576.

530   Griebel, A., D. M. Watson, and E. Pendall, 2017: Mistletoe, friend and foe: synthesizing ecosystem
531   implications of mistletoe infection. *Environmental Research Letters*.

532   Griebel, A., L. T. Bennett, D. S. Culvenor, G. J. Newnham, and S. K. Arndt, 2015: Reliability and
533   limitations of a novel terrestrial laser scanner for daily monitoring of forest canopy dynamics. *Remote*
534   *Sensing of Environment*, **166,** 205-213.

535   Hill, M. J., U. Senarath, A. Lee, M. Zeppel, J. M. Nightingale, R. D. J. Williams, and T. R. McVicar,
536   2006: Assessment of the MODIS LAI product for Australian ecosystems. *Remote Sensing of*
537   *Environment*, **101,** 495-518.

538   Hinko-Najera, N., and Coauthors, 2017: Net ecosystem carbon exchange of a dry temperate eucalypt
539   forest. *Biogeosciences*, **14,** 3781-3800.

540   Hutyra, L. R., and Coauthors, 2007: Seasonal controls on the exchange of carbon and water in an
541   Amazonian rain forest. *Journal of Geophysical Research: Biogeosciences*, **112**.

542   Isaac, P., J. Cleverly, I. McHugh, E. van Gorsel, C. Ewenz, and J. Beringer, 2017: OzFlux Data:
543   Network integration from collection to curation. *Biogeosciences*, **14,** 2903.

544   Jones, T. L., D. E. Tucker, and D. R. Ort, 1998: Chilling delays circadian pattern of sucrose phosphate
545   synthase and nitrate reductase activity in tomato. *Plant Physiology*, **118,** 149-158.

546   Karan, M., and Coauthors, 2016: The Australian Supersite Network: a continental, long-term
547   terrestrial ecosystem observatory. *Science of the Total Environment*, **568,** 1263-1274.

548   Keeling, C. D., S. C. Piper, R. B. Bacastow, M. Wahlen, T. P. Whorf, M. Heimann, and H. A. Meijer,
549   2001: Exchanges of atmospheric CO2 and 13CO2 with the terrestrial biosphere and oceans from 1978
550   to 2000. I. Global aspects. *Scripps Institution of Oceanography*.

551   Keith, H., E. van Gorsel, K. L. Jacobsen, and H. A. Cleugh, 2012: Dynamics of carbon exchange in a
552   Eucalyptus forest in response to interacting disturbance factors. *Agricultural and Forest Meteorology*,
553   **153,** 67-81.

554   Knauer, J., C. Werner, and S. Zaehle, 2015: Evaluating stomatal models and their atmospheric
555   drought response in a land surface scheme: A multibiome analysis. *Journal of Geophysical Research:*
556   *Biogeosciences*, **120,** 1894-1911.

557   Knauer, J., and Coauthors, 2017: Towards physiologically meaningful water-use efficiency estimates
558   from eddy covariance data. *Global Change Biology*.

559   Kolari, P., H. K. Lappalainen, H. Hänninen, and P. Hari, 2007: Relationship between temperature and
560   the seasonal course of photosynthesis in Scots pine at northern timberline and in southern boreal zone.
561   *Tellus B*, **59,** 542-552.

562   Kormann, R., and F. X. Meixner, 2001: An analytical footprint model for non-neutral stratification.
563   *Boundary-Layer Meteorology*, **99,** 207-224.

564   Lim, P. O., H. J. Kim, and H. Gil Nam, 2007: Leaf senescence. *Annu. Rev. Plant Biol.*, **58,** 115-136.

565   Lindroth, A., L. Klemedtsson, A. Grelle, P. Weslien, and O. Langvall, 2008: Measurement of net
566   ecosystem exchange, productivity and respiration in three spruce forests in Sweden shows
567   unexpectedly large soil carbon losses. *Biogeochemistry*, **89,** 43-60.

568   Lloyd, J., and J. A. Taylor, 1994: ON THE TEMPERATURE-DEPENDENCE OF SOIL
569   RESPIRATION. *Functional Ecology*, **8,** 315-323.

570   Medlyn, B. E., and Coauthors, 2011: Reconciling the optimal and empirical approaches to modelling
571   stomatal conductance. *Global Change Biology*, **17,** 2134-2144.

572   Mitscherlich, E. A., 1909: Das Gesetz des Minimums und das Gesetz des abnehmenden
573   Bodenertrages. *Landw. Jahrb*, **38,** 537-552.

574   Moncrieff, J., R. Clement, J. Finnigan, and T. Meyers, 2004: Averaging, detrending, and filtering of
575   eddy covariance time series. *Handbook of micrometeorology*, Springer, 7-31.

576   Moncrieff, J. B., and Coauthors, 1997: A system to measure surface fluxes of momentum, sensible
577   heat, water vapour and carbon dioxide. *Journal of Hydrology*, **189,** 589-611.

578   Monteith, J. L., 1965: Evaporation and environment. *Symp. Soc. Exp. Biol*, 4.

579   Moore, C. E., T. F. Keenan, R. A. Duursma, A. I. van Dijk, L. B. Hutley, J. R. Taylor, and M. J.
580   Liddell, 2016: Reviews and syntheses: Australian vegetation phenology: new insights from satellite
581   remote sensing and digital repeat photography. *Biogeosciences*, **13,** 5085.

582   Munné-Bosch, S., and L. Alegre, 2004: Die and let live: leaf senescence contributes to plant survival
583   under drought stress. *Functional Plant Biology*, **31,** 203-216.

584   Novick, K. A., A. C. Oishi, E. J. Ward, M. B. S. Siqueira, J. Y. Juang, and P. C. Stoy, 2015: On the
585   difference in the net ecosystem exchange of CO2 between deciduous and evergreen forests in the
586   southeastern United States. *Global Change Biology*, **21,** 827-842.

587   Novick, K. A., and Coauthors, 2016: The increasing importance of atmospheric demand for
588   ecosystem water and carbon fluxes. *Nature Climate Change*, **6,** 1023-1027.

589   Pan, Y., and Coauthors, 2011: A large and persistent carbon sink in the world's forests. *Science*, **333,**
590   988-993.

591   Pook, E., 1984: Canopy dynamics of Eucalyptus maculata Hook. II. Canopy leaf area balance.
592   *Australian Journal of Botany*, **32,** 405-413.

593   Poulter, B., and Coauthors, 2014: Contribution of semi-arid ecosystems to interannual variability of
594   the global carbon cycle. *Nature*, **509,** 600-603.

595   Prior, L. D., and D. M. Bowman, 2014: Big eucalypts grow more slowly in a warm climate: evidence
596   of an interaction between tree size and temperature. *Global change biology*, **20,** 2793-2799.

597   Reich, P. B., D. S. Falster, D. S. Ellsworth, I. J. Wright, M. Westoby, J. Oleksyn, and T. D. Lee, 2009:
598   Controls on declining carbon balance with leaf age among 10 woody species in Australian woodland:
599   do leaves have zero daily net carbon balances when they die? *New Phytologist*, **183,** 153-166.

600   Resco de Dios, V., A. W. Fellows, R. H. Nolan, M. M. Boer, R. A. Bradstock, F. Domingo, and M. L.
601   Goulden, 2015: A semi-mechanistic model for predicting the moisture content of fine litter.
602   *Agricultural and Forest Meteorology*, **203,** 64-73.

603   Restrepo-Coupe, N., and Coauthors, 2016: MODIS vegetation products as proxies of photosynthetic
604   potential along a gradient of meteorologically and biologically driven ecosystem productivity.
605   *Biogeosciences*, **13,** 5587-5608.

606   Restrepo-Coupe, N., and Coauthors, 2017: Do dynamic global vegetation models capture the
607   seasonality of carbon fluxes in the Amazon basin? A data-model intercomparison. *Global change*
608   *biology*, **23,** 191-208.

609   Saleska, S. R., and Coauthors, 2003: Carbon in Amazon forests: unexpected seasonal fluxes and
610   disturbance-induced losses. *Science*, **302,** 1554-1557.

611   Schimel, D. S., and Coauthors, 2001: Recent patterns and mechanisms of carbon exchange by
612   terrestrial ecosystems. *Nature*, **414,** 169-172.

613   Thom, A., 1972: Momentum, mass and heat exchange of vegetation. *Quarterly Journal of the Royal*
614   *Meteorological Society*, **98,** 124-134.

615   Tjoelker, M. G., J. Oleksyn, and P. B. Reich, 2001: Modelling respiration of vegetation: evidence for
616   a general temperature-dependent Q10. *Global Change Biology*, **7,** 223-230.

617   Trenberth, K. E., 1983: What are the seasons? *Bulletin of the American Meteorological Society*, **64,**
618   1276-1282.

619   van Gorsel, E., and Coauthors, 2013: Primary and secondary effects of climate variability on net
620   ecosystem carbon exchange in an evergreen Eucalyptus forest. *Agricultural and Forest Meteorology*,
621   **182-183,** 248-256.

622   Vickers, D., and L. Mahrt, 1997: Quality control and flux sampling problems for tower and aircraft
623   data. *Journal of Atmospheric and Oceanic Technology*, **14,** 512-526.

624   Webb, E. K., G. I. Pearman, and R. Leuning, 1980: Correction of flux measurements for density
625   effects due to heat and water vapour transfer. *Quarterly Journal of the Royal Meteorological Society*,
626   **106,** 85-100.

627   Wilczak, J. M., S. P. Oncley, and S. A. Stage, 2001: Sonic anemometer tilt correction algorithms.
628   *Boundary-Layer Meteorology*, **99,** 127-150.

629   Wilson, K., and Coauthors, 2002: Energy balance closure at FLUXNET sites. *Agricultural and Forest*
630   *Meteorology*, **113,** 223-243.

631   Wilson, K. B., D. D. Baldocchi, and P. J. Hanson, 2001: Leaf age affects the seasonal pattern of
632   photosynthetic capacity and net ecosystem exchange of carbon in a deciduous forest. *Plant Cell and*
633   *Environment*, **24,** 571-583.

634   Windsor, D. M., 1990: Climate and moisture variability in a tropical forest: long-term records from
635   Barro Colorado Island, Panama.

636   Wu, J., and Coauthors, 2016: Leaf development and demography explain photosynthetic seasonality
637   in Amazon evergreen forests. *Science*, **351,** 972-976.

638   Xia, J. Y., and Coauthors, 2015: Joint control of terrestrial gross primary productivity by plant
639   phenology and physiology. *Proceedings of the National Academy of Sciences of the United States of*
640   *America*, **112,** 2788-2793.

641 Yi, C., and Coauthors, 2010: Climate control of terrestrial carbon exchange across biomes and
642 continents. *Environmental Research Letters*, **5,** 034007.

643 Zhang, Y., Z. Tan, Q. Song, G. Yu, and X. Sun, 2010: Respiration controls the unexpected seasonal
644 pattern of carbon flux in an Asian tropical rain forest. *Atmospheric Environment*, **44,** 3886-3893.

645